Operational Aspects of Perovskite Chromite-based Fuel Electrode in Solid Oxide Electrolysis Cells (SOEC)

Diana M. Amaya-Dueñas[a], Matthias Riegraf[a], Andreas Nenning[b], Alexander K. Opitz[b], Rémi Costa[a*], and K. Andreas Friedrich[a,c]*

[a] German Aerospace Center (DLR), Institute of Engineering Thermodynamics, Pfaffenwaldring 38-40, D-70569 Stuttgart, Germany

[b] Institute of Chemical Technologies and Analytics, TU Wien, Getreidemarkt 9, A-1060 Vienna, Austria

[c] Institute of Building Energetics, Thermal Engineering and Energy Storage (IGTE), University of Stuttgart, Pfaffenwaldring 31, D-70569 Stuttgart, Germany

[*] E-mail: diana.amayaduenas@dlr.de ; remi.costa@dlr.de

ABSTRACT

The lanthanum strontium chromite perovskite $La_{0.65}Sr_{0.3}Cr_{0.85}Ni_{0.15}O_{3-\delta}$ (L65SCrN) was implemented as fuel electrode in electrolyte supported cells (ESC). The electrochemical cell performance in steam electrolysis operation with a fuel gas mixture of 80% H_2O - 20% H_2 was demonstrated to be comparable to Ni-CGO-based state-of-the-art cells at 860 °C. At 830 °C, 800 °C and 770 °C, the perovskite fuel electrode exhibited a gain in performance. Lower apparent activation energy barrier values were calculated for the L65SCrN in symmetrical and full configurations in contrast to Ni-CGO fuel electrodes. A reaction model is proposed, where the water splitting reaction mainly occurs on the oxygen vacancy sites on the L65SCrN surface, and where the exsolved metallic Ni nanoparticles assist the catalytic activity of the electrode with hydrogen

spillover and H_2 desorption. A voltage degradation of ~ 48 mV/ 1000h was calculated during 1000 hours in steam electrolysis operation at 860 °C close to thermoneutral voltage. Van-der-Pauw conductivity measurements corroborated this degradation with a decrease over time of the perovskite's p-type conductivity which appeared to be a diffusion-limited phenomenon. Nevertheless, the lower activation energy of perovskite-based fuel electrode for solid oxide cells (SOCs) is promising for green hydrogen production via steam electrolysis at reduced temperature and without the need of hydrogen sweep.

KEY WORDS: High temperature electrolysis, solid oxide electrolysis cell, green hydrogen, fuel electrode, perovskite, chromite, p-type, conductivity.

1. INTRODUCTION

Water electrolysis powered with electricity from renewable sources is a promising pathway to green hydrogen production.[1] The various electrolysis processes can be classified into two main categories: i) the low temperature technologies (LTE) that include mainly alkaline electrolysis (AE) and proton exchange membrane electrolysis (PEMEL), which both make use of liquid water at an operating temperature below 100 °C; and ii) the high temperature technologies (HTE), which operate typically with ceramic cells at temperatures above 600 °C to convert steam into hydrogen. Due to a different state of the water at these operating temperature, the thermoneutral voltage for these technologies corresponds to 1.47 V for LTE and 1.29 V for HTE.[2] Typically, the operating voltage for the LTE technologies is ~ 1.8 V, while the HTE can be operated at ~ 1.3 V. Since a significant amount of the energy required for the water splitting is supplied in the form of heat in HTE, these systems yield a lower specific electrical energy consumption in comparison to the LTE. While AE systems require 47 – 65 kWh / kg H_2 and PEMEL about 50 – 76 kWh / kg H_2, HTE systems offer the highest electrical efficiency with a consumption of ca. 40 – 44 kWh / kg H_2.[3] Moreover, typical high temperature cells, i. e. solid oxide cells (SOC) are unique due to their reversibility (rSOC). Such systems can either be operated with solid oxide electrolysis cells (SOECs) to convert sustainable electricity into chemical energy (in the form of green hydrogen, fuels or chemicals). Or as a

solid oxide fuel cells (SOFCs) to convert directly such chemical energy back into electricity.[4] This allows the versatile use of large storage-power generation units, which would require only one type of cells (rSOCs) and not separate Power-to-Fuel (electrolysis mode) and Fuel-to-Power (fuel cell mode) systems.[4] In solid oxide electrolysis (SOE), the water splitting reaction occurs at the fuel electrode of the SOC, as shown in Eq 1:[5]

$$H_2O + 2e^- \rightarrow H_{2(g)} + O^{2-}_{Electrolyte} \quad (1)$$

Since the electrode kinetics are enhanced owing to the high temperature,[6, 7] the use of PGM (Platinum Group Metal) catalysts typically used in PEMEL is avoided. State-of-the-art SOC fuel electrode materials are porous nickel-based cermets due to their high electrical conductivity. The stable catalytic activity of both metallic nickel phase (towards H_2 dissociation) and ceramic ceria-based phase (towards H_2O splitting and re-combination), enables reversible operation.[8, 9] In cathode supported cells (CSC), nickel is traditionally mixed with yttria stabilized zirconia (YSZ) into Ni-YSZ composite fuel electrodes, while it is more commonly found in combination with gadolinium-doped ceria (CGO), in the form of Ni-CGO cermets in electrolyte supported cells (ESC). However, when operated in electrolysis, nickel cermet electrodes are prone to irreversible degradation processes. Data from several studies suggest that the main issues correspond to:

i) Nickel agglomeration at high temperature. This may yield a loss of percolation in the cermet and a reduction of the active triple-phase-boundary (TPB) lengths.

ii) Nickel migration away from the interface between the electrolyte – fuel electrode. This is especially sensitive in CSCs at high temperatures, high overpotentials and high relative humidity, i.e. high pH_2O.[10-13] Some studies suggest the formation of $Ni(OH)_2$ volatile species in gas mixtures of H_2 and H_2O, that could be transported and re-precipitated in other locations within the fuel electrode.[14-16] Moreover, others also explain this microstructure evolution under electrolysis conditions by a polarization dependent interfacial energy between Ni and the oxide ion conducting phase, thus for example affecting the Ni wettability on the oxide surface.[17-19]

iii) Structural damage of the cell – especially in CSC – during redox cycles. Such event may affect the nickel percolation and even lead to cell failure by electrolyte fracture.[20] As a consequence, once the nickel cermet electrodes are activated i.e. when the NiO has been reduced into metallic nickel, there is the need to keep the electrode chemically reduced. Therefore, small amounts of hydrogen are added to the steam feed.

iv) Carbon deposition in H_2O + CO_2 co-electrolysis and dry CO_2 electrolysis operation. This is especially critical in CSCs with Ni-YSZ electrodes. However, the mixed ionic and electronic transport properties of ceria-based materials grant a superior tolerance against carbon formation to Ni-CGO composites in ESCs.[21]

Such contingencies in electrolysis operation with high pH_2O are inherent to the use of metallic nickel as electrocatalyst, current collector and, in the case of CSCs as structural component. Besides these technical divers, the International Energy Agency (IEA) recently classified nickel as critical raw material for the energy transition,[22] because of the increased demand in other technologies like batteries and AE, among others. Hence, such classification represents an additional driver for finding nickel substitutes. In regard to the HTE technologies, these issues drive the development of alternative fuel electrodes that could compete with the Ni-cermets on SOECs. Among the most important requirements on the use and implementation of such alternative fuel electrodes are: (i) promising catalytic activity, (ii) good electric conductivity and (ii) high dimensional and chemical stability in dual atmospheres with high steam and high hydrogen contents.

As alternative mixed ionic and electronic conductors (MIEC) such as the perovskite-based oxides (ABO_3) have attracted considerable interest due to their remarkable stability in reducing and oxidizing conditions. Despite their limited mechanical properties when compared to nickel cermets, perovskite-based electrodes are well-suited for ESC designs.[23] Their electro-catalytic properties can be tuned by a wide range of element combination on the A-site with lanthanides and alkaline-earth metals and also on the B-site with transition metals such as Mn, Co, Fe, Ni, Cr and Ti.[24] Particularly promising performance in steam electrolysis at 800 °C (-0.9 A•cm^{-2} at 1.3 V) has been shown with strontium titanates fuel electrodes with precipitation of metallic nanoparticles of Ni and Fe on the perovskite surface.[25] Such precipitation of

catalytically active metals, that are embedded in the perovskite lattice under oxidizing conditions, and then are exsolved as metallic nanoparticles on the perovskite surface under cathodic polarization and/or chemical reduction, is often denoted as exsolution.[8, 25-27]

Lanthanum chromites, that are p-type conductors, have also been investigated as electrocatalysts since reducible 3d transition metals (M) can be hosted on the B-site, yielding a large family of compounds with the general formula (La,Sr)(Cr,M)O_3. Various stoichiometric formulations as well as A-site deficient chromites have been recently investigated in H_2O electrolysis, CO_2 electrolysis and co-electrolysis.[8, 27-29] A-site deficient formulations were demonstrated to be more favorable for metal exsolution due to the high cation and oxygen vacancy concentration that partially destabilizes the perovskite lattice. In reducing conditions, some of the B-site cations are reduced to metals and exsolved on the surface maintaining the charge balance of the host perovskite lattice.[30]

In our recent work, we studied the lanthanum chromite $La_{0.65}Sr_{0.3}Cr_{0.85}Ni_{0.15}O_{3-\delta}$ fuel electrode decorated with exsolved Ni nanoparticles for SOC applications. Promising and comparable performance with respect to the typical nickel cermet fuel electrodes in ESCs was achieved.[8] Post-test analysis after 950 hours at high temperature H_2O and CO_2 co-electrolysis operation suggested remarkable dimensional stability of the Ni exsolved nanoparticles in the tested conditions.[8]

Most of the research and development efforts reported so far focused on tuning the composition of the chromite electrodes. However, very little is known about the operational aspects and benefits that such fuel electrode materials could provide to high temperature electrolysis cells over the traditional cermets. Data about the comparative assessment of perovskite-based electrodes with state-of-the-art fuel electrodes are limited. Therefore, the main objective of this work is to identify operational benefits for SOE operation by using perovskite-based fuel electrode cells instead of the traditional state-of-the-art Ni-CGO cermets in ESCs. The performance of $La_{0.65}Sr_{0.3}Cr_{0.85}Ni_{0.15}O_{3-\delta}$ (L65SCrN) and Ni-CGO fuel electrodes are evaluated, as well as the temperature dependency of the electrochemical performance of the L65SCrN-based cells between 770 °C and 860 °C. For the latter cells, the durability in steam electrolysis operation was investigated for 1000 hours.

2. EXPERIMENTAL METHODS

2.1 Cells preparation. ESCs were investigated in two different configurations: symmetrical button-cells and full square-cells implementing the perovskite fuel electrode L65SCrN.

2.1.1 L65SCrN symmetrical button-cell manufacturing. A chromite powder with nominal composition $La_{0.65}Sr_{0.3}Cr_{0.85}Ni_{0.15}O_{3-\delta}$ (L65SCrN) was synthetized by the nitrate combustion method.[8] SEM imaging of this powder is shown in the supporting information (SI) in Figure S1. The fuel electrode ink was prepared by dispersing the L65SCrN powder in a liquid ink vehicle (94 wt% α-Terpineol and 6 wt% ethyl cellulose) with a powder to liquid ratio of 2:1, and mixed with the 3-roll mill EXAKT 80E EL. The device Aurel model 900 (Aurel automation s.p.a, Italy) was used for the screen printing of the electrodes.[8] Symmetrical button-cells were prepared by screen printing 10 mm diameter circles of the L65SCrN ink on 20 mm-diameter commercial electrolytes CGO20 (5 µm) | 3YSZ (90 µm) | CGO20 (5 µm) from Kerafol GmbH (Eschenbach, Germany) and after drying heated up at 3 °C/min to 1200 °C in air and fired for one hour. Platinum paste was used as current collector and hand-brushed on both electrode surfaces. Following, the cells were heated up at 3 °C/min to 1050 °C in air and held also for one hour. The active electrode area was 0.785 cm^2.

2.1.2 Full-cell manufacturing. For these cells, the L65SCrN ceramic powder was supplied by Marion Technologies[31] (Verniolle, France) as shown in Figure S2. With this commercial powder, a L65SCrN ink was prepared as described above. Full cells were prepared by screen printing an area of 40 mm x 40 mm of the L65SCrN fuel electrode ink on 50 mm x 50 mm commercial electrolytes from Kerafol CGO20 (5 µm) | 3YSZ (90 µm) | CGO20 (5 µm). Then, those half-cells were fired in air at 1100 °C for one hour with a heating rate of 3 °C/min. Next, an area of 40 mm x 40 mm of the $La_{0.58}Sr_{0.4}Fe_{0.8}Co_{0.2}O_{3-\delta}$ (LSCF) oxygen electrode (Heraeus commercial reference) was printed on the other side of the electrolytes. The LSCF-printed electrode was co-fired in air with the brushed-platinum paste on the fuel electrode at 1050 °C for one hour. Moreover, state-of-the-art cells supplied by Sunfire GmbH (Dresden, Germany) with Ni-CGO cermet were used as reference. Apart from the fuel electrode, the cells were of the same architecture and

employed the same electrolyte substrate as the L65SCrN-based cells in this work. For the oxygen electrode, a LSCF/CGO composite with a LSCF current collector layer was used.

2.2 Symmetrical cells characterization. Symmetrical button-cells were tested at open circuit voltage (OCV) in a single chamber configuration at 860 °C, 830 °C, 800 °C and 770 °C with humidified H_2 flow. In order to minimize the gas diffusion contribution to the ASR of the symmetrical cells, electrochemical tests were carried out at a reduced pressure of ca. 295 mbar (10% H_2O – 90% H_2) and ca. 79 mbar (38% H_2O – 62% H_2). The pressure was regulated by continuous pumping of the chamber with a continuous feed gas flow rate of 0.02 slpm. The electrodes were contacted with highly porous Ni foams in a testing chamber of fused silica. These measures decrease the gas diffusion ASR to roughly 0.01 Ω cm^2.[32, 33] Four button cells were measured at the same time by using a multiplexing setup.[32] Electrochemical impedance spectroscopy (EIS) was performed in four-wire mode with a Novocontrol Alpha impedance analyzer in a frequency range from 50 mHz to 100 kHz and amplitude of the voltage stimulus of 50 mV. Equivalent circuit model fitting of the impedance data was performed with the commercially available program Zview®.[34]

2.3 Full cells characterization. The electrochemical characterizations of the L65SCrN fuel electrode implemented in a full ESC and the Ni-CGO reference cell were carried out on a high-temperature cell-test bench.[8, 11] The L65SCrN fuel electrode was contacted with a platinum mesh and the Ni-CGO with a nickel mesh. For both types of cells, the oxygen electrode was contacted with a gold mesh. A sealing gold frame was applied and the cells were heated at a rate of 3 °C/min to 900 °C with N_2 (1 slpm) on the fuel side and with air (1 slpm) on the oxygen side respectively, to ensure gas-tightness of the gold seal. Then, the fuel electrodes were reduced with H_2 (1 slpm) for one hour at 900 °C. Afterwards, the operating cell temperature was adjusted to 860 °C, 830 °C, 800 °C and 770 °C. For each temperature the fuel gas composition was set to 80% H_2O – 20% H_2 (0.8 slpm of H_2O and 0.2 slpm of H_2) and polarization curves (i-V) were measured from OCV to 1.5 V at a rate of -0.012 A•s^{-1}. Galvanostatic EIS measurements were performed at OCV with the electrochemical workstation SP-200 from BioLogic Science Instruments, at a frequency range from 50 mHz to 100 kHz and an AC amplitude of 500 mA. To avoid the scattering of the EIS data at low frequencies

caused by fluctuations from the steam supply, the fuel gas was diluted with 0.5 slpm of N_2 during the impedance measurements. Subsequently, a galvanostatic durability test of ~ 1000 hours on the L65SCrN fuel electrode cell with a fuel gas composition of 80% H_2O – 20% H_2 (0.8 slpm of H_2O and 0.2 slpm of H_2) at 860 °C was carried out. The current density was fixed to -0.67 A•cm^{-2}. EIS measurements at OCV were carried out in a specific time interval. Equivalent circuit model fitting of these data was performed with Zview®.[34] After such long-term SOE operation, the L65SCrN fuel electrode cell's morphology was observed with a scanning electron microscope (SEM) Zeiss ULTRA PLUS SEM (Carl Zeiss AG, Germany) in combination with energy-dispersive X-ray spectroscopy (EDS) for elemental analysis, with a Bruker Xflash 5010 detector supported with the software Quantax 400. The crystalline structure was investigated by X – ray diffraction (XRD) using the D8 Discover GADDS, equipped with a VÅNTEC-2000 area detector (Bruker AXS, Germany) and a microfocus Cu-Kα radiation source operated at 50 kV and 0.6 mA with Bragg-Brentano geometry. Crystalline phases were identified with the ICDD database.

2.4 Conductivity measurements. The electrical conductivity was measured on porous L65SCrN films that were screen-printed on inert, insulating 1x1 cm Al_2O_3 substrates, and subsequently sintered in air at 1100 °C for one hour with a ramp rate of 3 °C/min. On these, four-wire Van-der-Pauw measurements[35] were performed to determine the sheet resistance and effective conductivity in varying gas mixtures and temperatures in a high-temperature measurement chamber consisting of a fused silica tube inside a tubular furnace. As feed gases, humidified argon (pH_2O ~ 25 mbar), 2.4 % H_2-Ar and oxygen were mixed in a 4:1 ratio at a total flow rate of 500 sccm. Although the partial pressures of H_2 and H_2O were much smaller during the Van-der-Pauw measurements, the resulting pO_2 (which is a function of the mixing ratio) was equal to that in the SOE full cell tests (~10^{-16} bar). Therefore, the defect chemistry and Ni exsolution kinetics were comparable to the full cell electrolysis measurements (80% H_2O – 20% H_2).

3. RESULTS AND DISCUSSION

3.1 Temperature dependency of the steam electrolysis with L65SCrN and Ni-CGO fuel electrodes in ESCs. Polarization curves of full cells with L65SCrN and Ni-CGO fuel electrodes in SOE operation are shown in Figure 1a. The fuel gas mixture was 80% H_2O - 20% H_2 and the operating temperature was varied

from 860 °C to 770 °C. At the typical SOE operating temperatures, the thermoneutral voltage for steam electrolysis remains relatively constant at 1.29 V. For both types of cells, the specific electrical energy requirement[36] close to thermoneutral voltage (1.29 V) was calculated to be ~ 35 kWh/kg H_2. This calculation was done as the ratio between the consumed power and the produced hydrogen mass flow, assuming Faraday efficiency of ~ 1.For stacks the values are typically slightly higher in the range between 37 – 44 kWh/ kg H_2.[3, 37] Regardless the fuel electrode and the temperature, the cell voltage U_{cell} showed a nearly linear evolution without indication of mass transport limitations in the investigated range. At 860 °C, a comparable performance of the two cells was appreciable. However, at lower temperatures, a significant performance difference was observed: at the thermoneutral voltage of ~1.29 V the Lc65SCrN-based cells displayed higher electrolysis current densities, i.e. 0.65, 0.52 and 0.40 A•cm^{-2}. In contrast, those values are 0.61, 0.48 and 0.37 A•cm^{-2} for the Ni-CGO cells at 830 °C, 800 °C and 770 °C respectively. Above 1.29 V, the curves flatten slightly, likely due to improved electrode kinetics and electrode/electrolyte transport characteristics because of the local heating when entering the exothermal regime.[38] Nonetheless, in first approximation, U_{cell} can be described by Ohm's law in Eq. 2 as a function of:

i) the OCV (U_{OCV}),

ii) the applied electrolysis current density J, and

iii) the area specific resistance of the cell (ASR_{total}) that is the slope of the polarization curves in the linear range, and which is a function of the operating temperature. The temperature dependency of the ASR_{total} can be described by an Arrhenius-type expression as shown in Eq. 3.

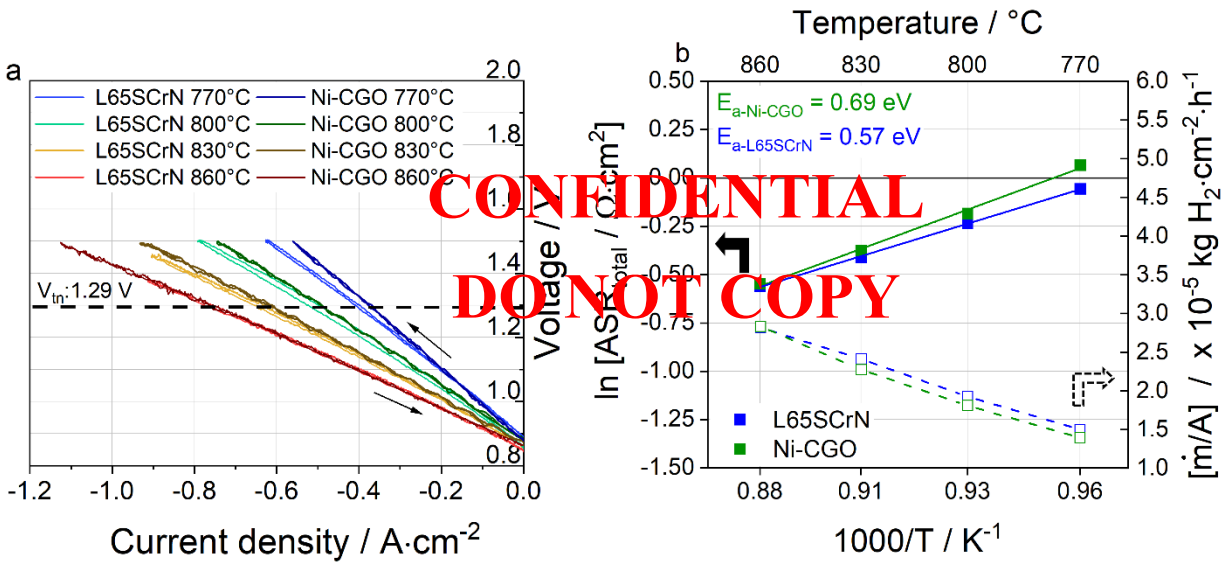

Figure 1. (a) Polarization curves of L65SCrN and Ni-CGO fuel electrodes on full ESCs in electrolysis mode with a fuel gas mixture of 80% H_2O - 20% H_2 (0.8 slpm of H_2O and 0.2 slpm of H_2) at 860 °C, 830 °C 800 °C and 770 °C. The thermoneutral voltage (1.29 V) of steam electrolysis is depicted. (b) Arrhenius-type plots of the ASR_{total} for the L65SCrN and Ni-CGO cells calculated from (a) on a linear interval close to the thermoneutral point. The corresponding normalized hydrogen production rate is shown on the right axis.

$$U_{cell} = U_{OCV} + ASR_{total} * J \quad (2)$$

$$ASR_{total} = B \exp\left(\frac{E_a}{RT}\right) \quad (3)$$

Figure 1b shows the Arrhenius-type plot of ASR_{total}. The exponential fits were shown to be suitable to describe the temperature dependency and thus it was possible to determine an apparent activation energy barrier E_a of the ASR_{total} for the two type of cells: $E_a = 0.57\ eV$ for the cells with L65SCrN fuel electrode ($R^2 > 0.999$) and $E_a = 0.69\ eV$ for the cells with Ni-CGO cermet electrode ($R^2 > 0.996$). The normalized hydrogen production rate $\frac{\dot{m}}{A}$ is also reported as complementary indicator of the performance (Figure 1b, right axis), with $\dot{m}$ as the calculated mass flow rate of produced hydrogen and A as the active area of the cell. At 860 °C both type of cells produced similar amount of hydrogen. However, at lower temperatures the hydrogen production rate calculated for the L65SCrN-based cell was systemically higher than the one

for the Ni-CGO-based cell. This observation correlates well with the lower apparent E_a calculated for the L65SCrN-based cell, which reflects lower ASR_{total} values at lower temperatures. To elucidate the different temperature dependencies of the two type of cells, it is thus necessary to further resolve the specific contributions of the ASR_{total}, which can be described as the sum of the ohmic and polarization resistance terms:[39]

$$ASR_{Total} = (ASR_{ohmic}) + \left(ASR_{polarization}\right) \qquad (4)$$

Considering the contribution of the electrolyte, the current collection and interfacial resistances (CCI) to the ohmic term, as well as the contributions to the polarization term from the fuel and oxygen electrode processes and the gas transport losses, Eq. 4 can be detailed as:

$$ASR_{Total} = \left(ASR_{electrolyte} + ASR_{CCI}\right) + \left(ASR_{fuel\ electrode} + ASR_{oxygen\ electrode} + ASR_{gas}\right) \quad (5)$$

The term corresponding to the gas transport losses mainly accounts for the gas conversion polarization along the gas channels of the cell housing and also due to the fuel utilization of 25 % at -1 A•cm^{-2}. The gas diffusion limitation (gas flow perpendicular to the fuel electrode) is expected to be minimal in the ESC architecture. Since the electrolyte and the oxygen electrode were similar for both type of cells, the difference in ASR_{total} can be attributed to the difference in fuel electrode and corresponding interfacial resistances. The thicknesses of both fuel electrodes were of the same order of magnitude, L65SCrN ~ 13 µm and Ni-CGO ~ 10 – 13 µm,[40] which is most likely thicker than the characteristic electrochemically active thickness. Hence, kinetics are co-limited by ion conduction and electrochemical reactions within the porous fuel electrode, and do not change with thickness variation.[32, 41, 42]

The specific response of each cell upon temperature variation was systematically investigated by EIS at OCV, with the aim of identifying the different impedance processes. Figure 2 shows imaginary impedance spectra for the (a) L65SCrN- and (b) Ni-CGO-based full cells at different temperatures. The characteristic frequencies of the charge transfer process on LSCF oxygen electrode and the LSCF/CGO interfacial double-layer capacitance were identified to be between 100 Hz and 1 kHz.[8, 43, 44] A low frequency peak, that is generally associated to the gas conversion in our setup[11] was identified at ~ 3 Hz. A slightly lower

frequency (~ 1 – 3 Hz) of the gas conversion was observed for the L65SCN electrodes, which is in agreement with our previous work with similar L65SCrN fuel electrodes.[8] The gas conversion resistance can be expected to slightly increase with higher temperature,[45] which is in accordance with the observed behavior for the L65CrN-based cell at frequencies ~1 Hz (Figure 2.a).

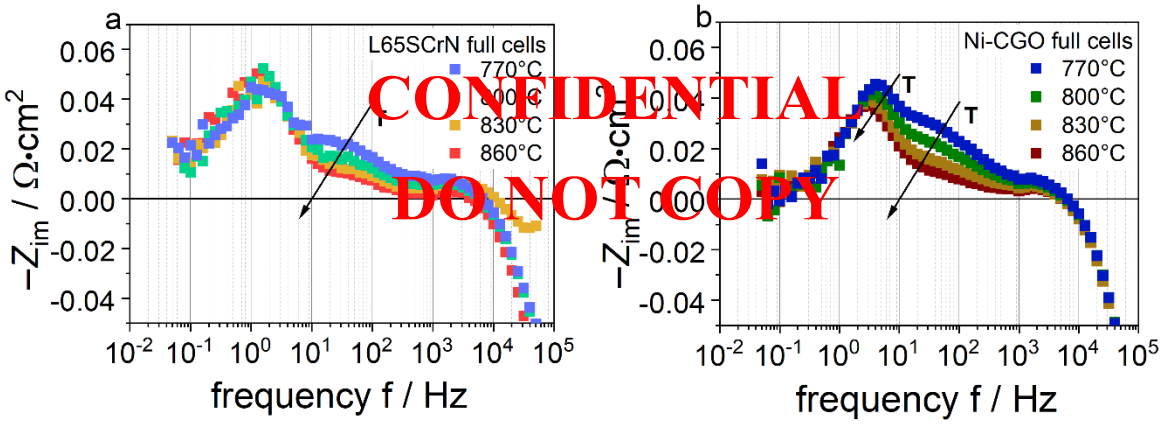

Figure 2. Imaginary impedance spectra recorded at OCV of (a) L65SCrN- and (b) Ni-CGO-based full ESCs in electrolysis mode with a fuel gas mixture of 80% H_2O - 20% H_2 (0.4 slpm of H_2O, 0.1 slpm of H_2 and 0.5 slpm N_2) at 860 °C, 830 °C, 800 °C and 770 °C.

However, the Ni/CGO-based cell showed an opposed temperature dependency of the impedance at frequencies of ~1 Hz, where the resistance decreased with increasing temperature (Figure 2.b). This behavior was possibly caused by an increased convolution of the gas conversion process and the Ni/CGO fuel electrode process at low temperatures. Moreover, the temperature variation showed a strong dependency of a process between 3-100 Hz for both cells, characterized by a decrement of the imaginary impedance upon temperature increase. These processes are likely linked to electrochemical polarization and surface oxygen exchange processes for both fuel electrode types, which is consistent with previous studies of L65SCrN[8] and Ni/CGO fuel electrodes.[46, 47] Nevertheless, these processes could overlap with the gas conversion at ~1 Hz.[40, 44, 48] Additionally, on porous electrodes, ion conduction, stoichiometry changes (chemical capacitance) and surface redox kinetics cannot be deconvoluted by individual frequencies. All of these phenomena make very difficult to precisely quantify the $ASR_{fuel\ electrode}$ term. What stands out from these spectra is the response of the imaginary impedance of the L65SCrN-based cell in the frequency

range between 1-100 Hz upon changing temperature, which was less pronounced than the one of the Ni/CGO-based cell, being thus in accordance with the trend observed on the polarization curves in Figure 1. In the Nyquist plots of these EIS spectra (Figure S3), a slight difference in the ohmic resistance between the L65SCrN and Ni-CGO-based cell can be observed for all temperatures. For each temperature, the perovskite-based cell exhibited a systematically higher ohmic resistance, with an increment of ~ 0.08 Ω•cm^2 with respect to the Ni-CGO cells. As an example, at 860 °C an ASR_{ohmic} of 0.46 Ω•cm^2 was identified for Ni-CGO, while 0.54 Ω•cm^2 for the L65SCrN cells. For the case at 770 °C, the ASR_{ohmic} for the Ni-CGO was identified at 0.86 Ω•cm^2 and for the L65SCrN at 0.94 Ω•cm^2. Such systematic difference in the ohmic resistance could be attributed to a lower electronic conductivity of the perovskite electrodes. A minor contribution to this difference might also originate from slightly different contact resistances between electrodes and current collectors. However, this can by far not explain the entire observed difference in the ohmic resistance. In order to better assess the fuel electrode processes on the L65SCrN fuel electrodes, the temperature dependency was evaluated in a symmetrical cell configuration in H_2: H_2O atmospheres as following.

3.2 Temperature and gas composition dependence of the polarization resistance of L65SCrN fuel electrodes. EIS measurements at OCV of L65SCrN symmetrical button-cells are shown in Figure 3 a-d, in which the Nyquist plots showed two semicircle-like features for all 4 temperatures and both gas compositions (Figure 3a and c). The low frequency process at peak frequencies of ~ 0.1 -1 Hz was likely related to a L65SCrN surface process.[8] In the symmetrical cell test setup, H_2 and H_2O partial pressures were lower and the atmosphere was more reducing, compared to the full cell setup. Therefore, due to the different oxygen stoichiometry in the symmetrical setup, the CGO buffer layer and the L65SCrN exhibit higher chemical capacitances, which could be modelled in parallel connection. Moreover, the surface kinetics are lower due to the lower H_2 and H_2O partial pressures, which leads to a decrement of the characteristic frequency, also due to the larger ASR and chemical capacitance. Consequently, for the symmetrical cells studied in this work, the characteristic frequency shifted to lower values, identified at ~ 0.4 – 0.6 Hz (Figure 3b and d). Equivalent circuit model (ECM) fitting was performed in order to estimate the resistance values

of the different thermally-activated contributions. Details of the ECM for each temperature are described in FiguremS4-S5 and Tables S1-S10. The fitted resistance values of the L65SCrN electrode polarization process as a function of temperature are shown in the Arrhenius-type plot in Figure 3e.

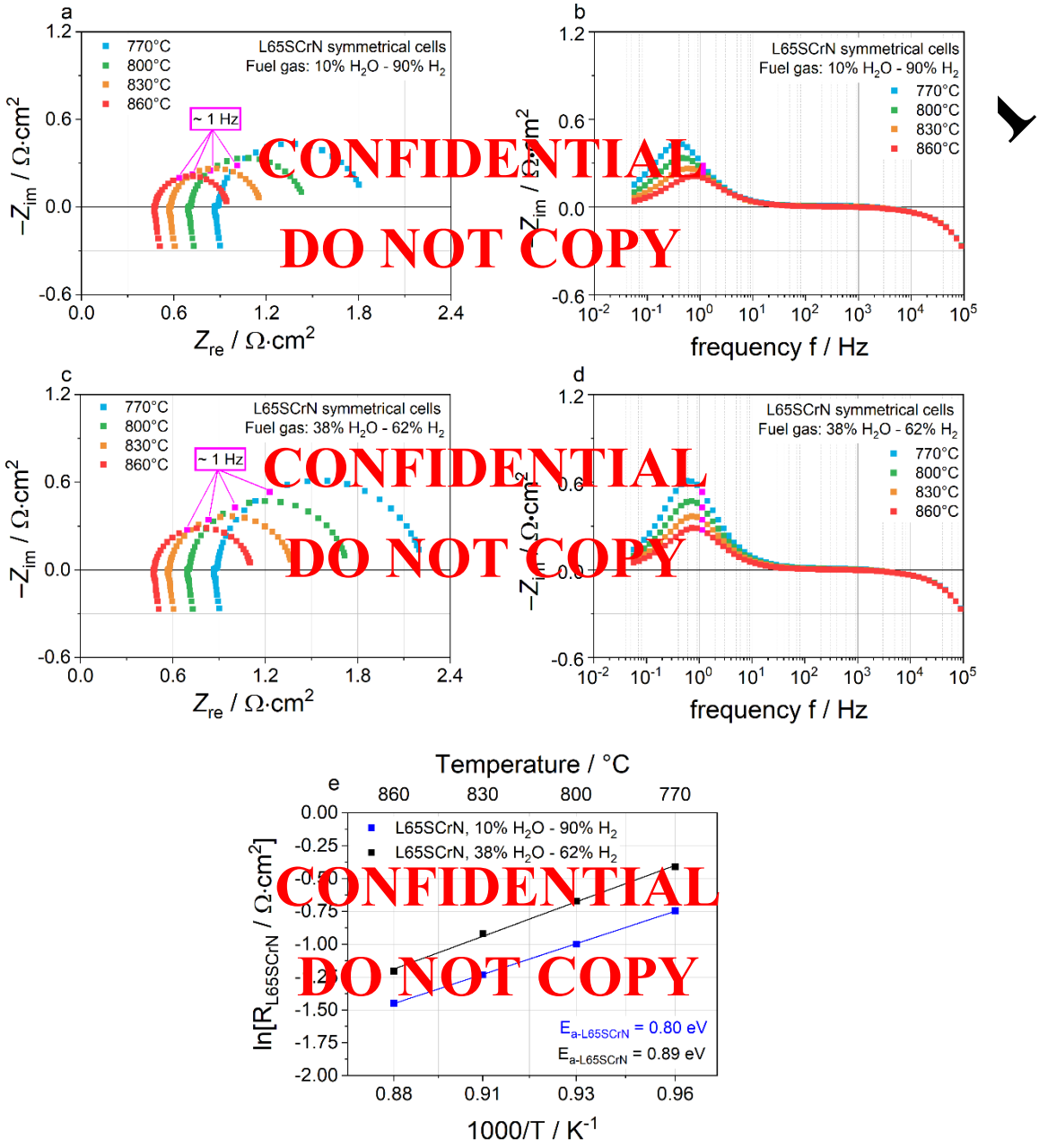

Figure 3. EIS spectra recorded at OCV of L65SCrN symmetrical cells at 860 °C, 830 °C, 800 °C and 770 °C. (a) Nyquist and (b) imaginary impedance plots for the fuel gas mixture of 10% H_2O - 90% H_2. (c)

Nyquist and (d) imaginary impedance plots for the fuel gas mixture of 38% H_2O - 62% H_2. (e) Arrhenius-type plots of L65SCrN symmetrical cells calculated from ECMs at OCV with fuel gas mixture of 10% H_2O - 90% H_2 (blue pattern) and 38% H_2O - 62% H_2 (black pattern).

Apparent activation energy barrier values E_a for the L65SCrN electrochemical processes were calculated from the Arrhenius-type relation.[49] The exponential fits were calculated with a single apparent activation energy barrier. These Arrhenius-type plots yielded an $E_a = 0.80\ eV$ ($R^2 > 0.999$) for the gas composition 10% H_2O - 90% H_2 and $E_a = 0.89\ eV$ ($R^2 > 0.997$) for 38% H_2O - 62% H_2. These similar values suggest that the mechanistic pathway is the same for both gas phase compositions with no significant influence of pH_2 on the nature of the rate-determining step between 90 % and 62 % H_2. Furthermore, these values are within the range of other perovskite-type MIEC fuel electrode materials (tested in H_2:H_2O mixtures), such as $Sr(Ti,Fe)O_{3-\delta}$ (STF),[50] as well as for CGO thin film electrodes.[51, 52] The calculated E_a values for the L65SCrN surface process are within the relatively broad range reported for Ni-CGO cermets ~ 0.51 – 1.16 eV in H_2:H_2O mixtures.[32, 48, 49, 53] Due to the similarity with the electrolyte substrates, the most suitable reference data for comparison are the results from the symmetrical cells Ni-CGO|CGO-3YSZ-CGO|Ni-CGO reported by Riegraf et al.[49] In their work, the authors calculated an apparent activation energy of ~ 1.16 eV for symmetrical Ni-CGO cells tested in 20% H_2O-80% H_2 between 600 °C and 900 °C.[49]

Overall, the calculated apparent activation energy depends not only on the energy barrier of the rate-limiting step, but further on temperature-dependent concentrations of surface adsorbates, oxygen vacancies and polarons. Because of the complexity of the deconvolution of these steps, a quantification of such activation energies would be very challenging and would require density functional theory (DFT) modelling, which goes beyond the scope of this work. Instead, one could assume that the calculated apparent E_a is probably related to a rate-limiting step, that has a different activation energy barrier for the L65SCrN than for the Ni-CGO. One important difference between the Ni-CGO cermet and the perovskite L65SCrN electrodes is the Ni dispersion. In Ni-CGO the Ni particles are percolating in the electrode and are much coarser than the exsolved Ni nanoparticles on the L65SCrN. Another relevant difference is the

ceramic phase: different intermediate steps could take place on the CGO surface in contrast to the L65SCrN surface.

Hence, it is reasonable to assume that the kinetics of the intermediate reaction steps are likely to be different. Nevertheless, what can be drawn from these results in correlation with the full cell measurements is that the kinetics of both electrodes are similar at 860 °C due to the comparable good cell performance. Below 860 °C the perovskite-based fuel electrodes show a gain in performance, which could possibly indicate that the reaction kinetics at these temperatures are more favorable on the L65SCrN than on the Ni-CGO fuel electrodes. Regarding perovskite electrodes, the reaction kinetics might be enhanced by metallic nanoparticles exsolved on the perovskite's surface. Such performance improvements have been reported on ferrite perovskites with exsolution of Fe[54, 55] and Ni.[56]

In our previous work,[31] we observed that sulfur species poisoned the metallic Ni on the L65SCrN surface in SOFC operation, for which we speculated that Ni is likely involved in the H_2 dissociation and perhaps also in a possible charge-transfer reaction at the TPB between gas phase/exsolved metallic Ni phase/perovskite phase.

Analogous to this, it was proposed on ferrite perovskites in SOFC operation that the water re-combination occurs on the perovskite surface and the hydrogen spill over the metal (Fe or Ni) exsolutions.[54] The authors also assumed that the dissociation of H_2 is much faster on the metal particles compared to the perovskite surface.[54]

For the reverse case, it has been reported that on CGO and ferrite perovskites the H_2O dissociation is much faster than the H_2 desorption.[57, 58] Consequently, despite the lack of data for L65SCrN reaction mechanisms in SOE operation, it is possible to consider that the Ni is assisting the electrode kinetics. This assumption is also in line with the results of a DFT study by Hansen and Wolverton, who investigated the kinetics and thermodynamics of H_2O dissociation on thin films of CeO_{2-x}(111) deposited on close-packed noble metal surfaces. They found that H_2 desorption exhibited a higher kinetic energy barrier on the ceria surface and therefore H_2 desorption was taking place via hydrogen spillover on the noble metal particles.[59]

Therefore, it is possible that hydrogen spillover from the L65SCrN surface to the metallic Ni particles would facilitate the hydrogen recombination and desorption in SOE operation.

As sketched in the mechanism in Figure 4, we propose that the adsorbed H_2O dissociates into proton H^+ and hydroxyl group OH^- on the perovskite surface, where the positively charged proton H^+ attaches to the lattice oxygen O_O^X to form a $OH_O^\bullet$ and the negatively charged hydroxyl group OH^- fills the positively charged oxygen vacancy $V_O^{\cdot\cdot}$ to form another $OH_O^\bullet$.[5] By means of an electron transfer, these two $2OH_O^\bullet$ are then electrochemically reduced to $2O_O^X$ and $2H_{ad}$. Then, hydrogen ad-atoms spill over from the perovskite surface to the exsolved metallic Ni, where finally $2H_{ad}$ desorbs as $H_{2(g)}$ away from the electrode. The electroneutrality of the perovskite lattice is maintained with one lattice oxygen O_O^X filling the oxygen vacancy $V_O^{\cdot\cdot}$ on the electrolyte, which is transported in the form of O^{2-} to the oxygen electrode,[5, 60] as suggested in Eq. 1.

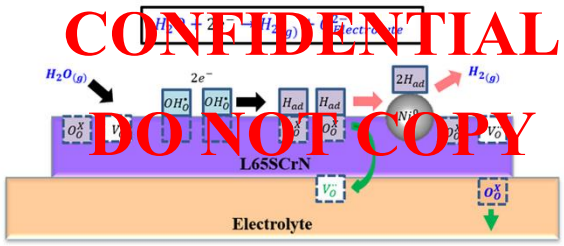

Figure 4. Sketch of the proposed model for the water splitting reaction with the oxygen vacancies on the L65SCrN fuel electrode. The hydrogen spillover, recombination and desorption take place on the metallic Ni nanoparticles exsolved on the perovskite surface.

3.3 On the long-term stability of L65SCrN fuel electrodes in SOE. The long-term behavior was evaluated during 1000 hours in galvanostatic conditions at 860 °C with a fixed electrolysis current density of -0.67 A•cm^{-2}, corresponding to the initial thermoneutral voltage of 1.29 V. Impedance measurements were carried out roughly each 100 hours at OCV (Figure 5). During the first 36 hours there was a performance improvement where the cell voltage decreased to 1.27 V. This improvement correlated with a strong shrinkage of the low frequency fuel electrode arc in the impedance spectra in Figure 5c and d. During this time, very likely the surface chemistry of the L65SCrN electrode changed due to electrolysis operation.

The most obvious candidate for this process is Ni exsolution ($Ni^{2+/0}$),[8] creating metallic surface particles that are catalytically more active for H_2 formation as the bare oxide surface. Also, the increment of the oxygen vacancy concentration may modify the hydration properties of the perovskite surface,[5] as well as the Cr species reduction ($Cr^{6+/4+}$ and $Cr^{4+/3+}$) and Sr migration. All together, these phenomena that are depending on the gas composition, cathodic overpotential and temperature, led possibly to an activation of the fuel electrode.

After this period, the voltage increase rate was estimated close to 48 mV/1000 h, which corresponds to a relative voltage increment $\Delta U/U_o$ of about 3.6 %. These results represent a degradation as twice as high as from Schefold et al., who reported 25 mV / 1000 h corresponding to $\Delta U/U_o$ of 1.7 %. Their results were measured in the first 1000 hours of operation of an ESC with a Ni-CGO fuel electrode operated in steam electrolysis (75 % H_2O) at 850 °C and -0.7 A•cm^{-2}. Over 8000 hours, they reported an average voltage drift of 5.1 mV / 1000 hours.[40]

ECM fitting was performed in order to quantify the evolution of both the ohmic and polarization resistances, as depicted in Figure 5.b. (Those ECMs are detailed in Table S11 and Figure S6). From the plot in Figure 5b and the Nyquist plot in Figure 5c, it is noticeable that the ohmic resistance shifts to higher values with time. Until an operation time of ca. 833 hours this value strongly increases by 9.4%, but then seems to stabilize at 0.58 Ω•cm^2. EIS recorded after 67 hours confirmed that the polarization resistance remained constant along the duration of the test at ca. 0.1 Ω•cm^2, which is in good agreement with our previous study, thus ratifying also the reproducibility of these results.[8] After 400 hours of operation, in an attempt to recover the ohmic resistance, a redox cycle was applied to the cell by flushing 0.1 slpm of oxygen for 1 hour on the fuel side. However, the ohmic resistance degraded continuously. In summary, the degradation processes mainly affected the ohmic resistance while the electrochemical electrode kinetics remained rather stable.

To identify any significant chemical changes of the L65SCrN electrode after the long-term test, microstructural investigations were performed. The SEM image Figure 6.a shows that there were no delamination at any of the interfaces, suggesting a good thermal and mechanical compatibility between the

different cell components. However, tiny cracks on the CGO barrier layer on the fuel electrode side are visible, for which an artifact from sample cleaving during metallographic preparation may not be excluded. Nevertheless, in the case that those cracks were generated under SOE operation, they would imply a decrease of the active cell area for the electrochemical reaction, which would increase both the ohmic and polarization resistances. In such a case, since the ohmic resistance represents most of the overall cell resistance, the expected changes in the polarization resistance would be hard to be observed and resolved.

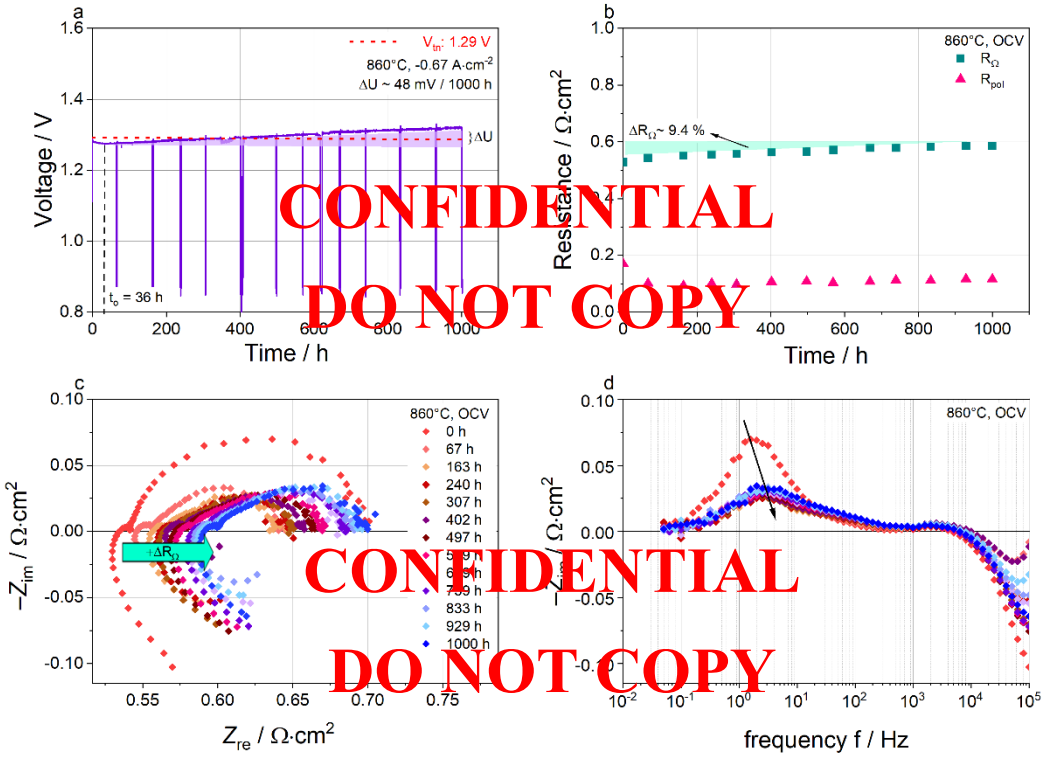

Figure 5. (a) Voltage vs. time during 1000 h long-term SOE with fuel gas mixture of 80% H_2O - 20% H_2 (0.8 slpm of H_2O and 0.2 slpm of H_2) at 860 °C and -0.67 A•cm^{-2} of L65SCrN fuel electrode in full ESC. (b) Fitted values of the evolution of the ohmic and polarization resistance during long-term study. (c) Nyquist plot and (d) imaginary impedance plot at OCV and 860 °C during long-term study of 1000 hours in SOE with fuel gas mixture 80% H_2O - 20% H_2 (0.8 slpm of H_2O and 0.2 slpm of H_2).

Elemental analysis performed by EDS revealed the presence of Sr and Zr within the CGO barrier layer, as well as distinctive morphologies within the L65SCrN layer correlate with presence of Ce and also Gd (Figure S7 and S9 and Table S12-S13 in the SI). These results could suggest the presence of a zirconate phase in the CGO barrier layer. Complementary to this, XRD characterizations were performed both at the inlet and the outlet of the fuel electrode. In Figure 6.b, the X-ray diffraction pattern at the outlet shows the identified characteristic peaks of the different components of the fuel electrode (L65SCrN, CGO20, 3YSZ and Pt). Nonetheless, these results did not reveal pertinent secondary phases nor phase decomposition, suggesting a zirconate phase was likely not relevant to explain the measured degradation.

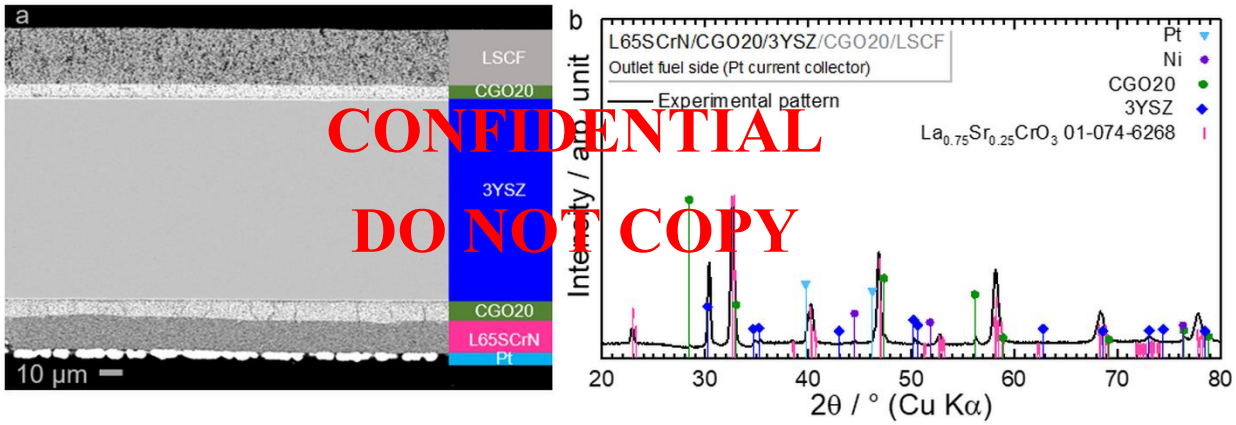

Figure 6. (a) Cross-section view of outlet side of an ESC implementing the L65SCrN fuel electrode after SOE operation at 860 °C for ca. 1000 hours. (b) XRD pattern of outlet side from ESC performed on the fuel electrode side Pt/L65SCrN/CGO/3YSZ after SOE operation at 860 °C for ca. 1000 hours.

With respect to the strong ohmic degradation, the effect of the cathodic overpotential on the L65SCrN transport properties should be cautiously considered. In electrolysis operation, the hydrogen partial pressure increases at high current densities while the oxygen potential in the perovskite is decreased, creating more oxygen vacancies. In p-type conductors, such as L65SCrN, the positively charged oxygen vacancies that are created under strongly reducing conditions would decrease the concentration of electron holes along the B-O-B chains in the perovskite lattice.[61, 62] Therefore, a possible decrease of the (electronic) conductivity could explain the observed increment of the ohmic resistance. Because of this observation, Van-der-Pauw conductivity measurements were performed on porous L65SCrN samples as shown in Figure 7.

3.4 L65SCrN conductivity assessment in SOE operating conditions. The pO_2 dependence of the conductivity was evaluated at ~ 860 °C for different oxygen partial pressures (Figure 7a). A $(pO_2)^{0.18}$ dependency was identified for the range between ~ 10^{-20} and 10^{-13} bar. This dependency is reasonably close to $(pO_2)^{0.17}$, which was measured on LSCrN formulations by Sauvet and Irvine[63] and by Yasuda and Hishinuma.[64] Meadowcroft reported $(pO_2)^{0.19}$ on undoped lanthanum chromites.[65] This behavior is compatible with the hole conduction in p-type conductors.

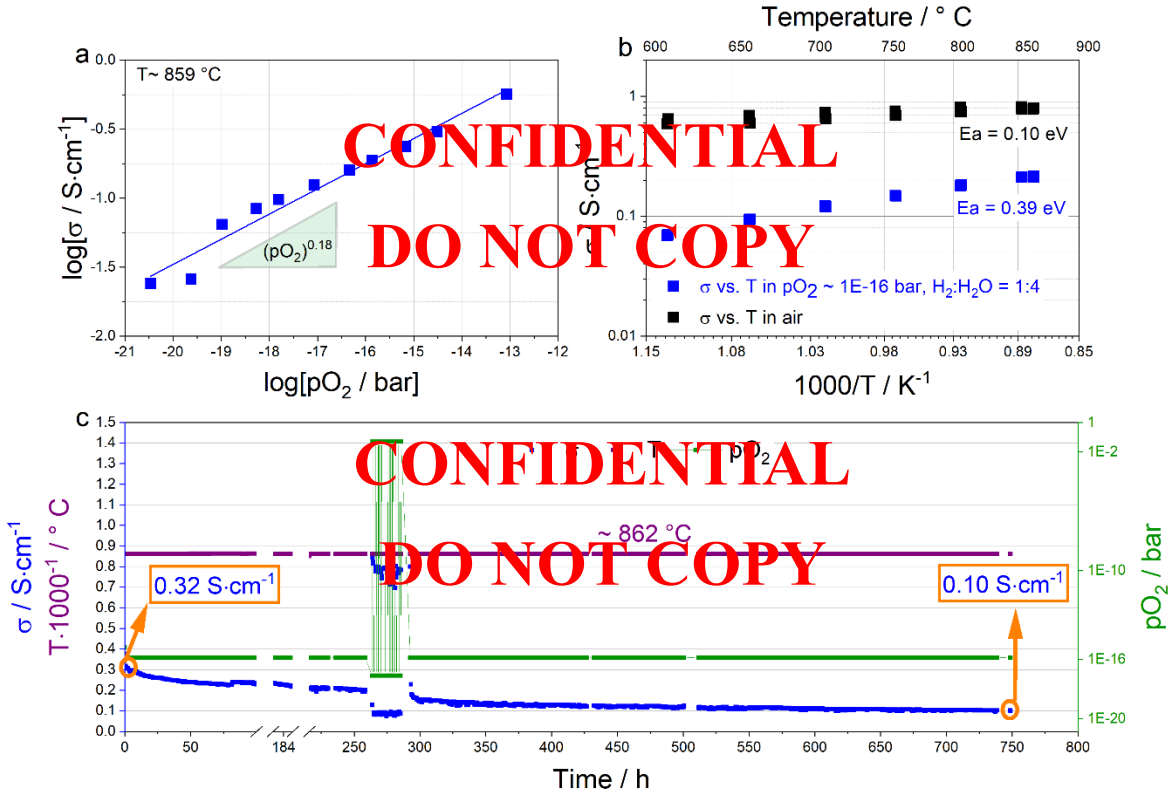

Figure 7. (a) Van-der-Pauw conductivity measurement of the L65SCrN conductivity vs. oxygen partial pressure at 859 °C. (b) L65SCrN conductivity vs. temperature in air (black dots) and also at constant oxygen partial pressure of ~ 10^{-16} bar (blue dots). (c) L65SCrN conductivity (blue dots), sample temperature (violet dots) and oxygen partial pressure (green dots) vs. time during 750h-durability test.

The temperature dependency in air (Figure 7b – black-colored data) yielded a value of $E_a = 0.10\ eV$, which agrees with the values between 0.11 eV and 0.14 eV reported in previous studies.[63, 64] For a better

comparison with the cell test in Figure 5, the conductivity measurement in reducing atmospheres was performed at a constant pO_2 of ~10^{-16} bar (H_2: H_2O mixing ratio of 1:4) between ~ 600 °C and 860 °C (Figure 7b – blue-colored data). The measured in-plane conductivity was as low as ~ 0.2 - 0.3 S•cm^{-1} at 860 °C, which was ~ 2 orders of magnitude lower in contrast to the reported values for the densely sintered bulk perovskite,[64] due to its tortuosity and lower volume fraction.[66] Also, the much smaller particle interface area (sintering neck) in a porous ceramic likely leads to a higher grain boundary resistance, which further decreases the conductivity.

At these reducing conditions, an apparent activation energy value of $E_a = 0.39\ eV$ was calculated. In constrast to the E_a estimation in air, this higher activation energy value could possibly give an insight on how the conductivity is affected in reducing atmospheres. In this p-type conductor, it is assumed that the holes (charge carriers h$^{\bullet}$) are present on the Cr-sites, such as $Cr^{4+} = Cr_{Cr}^{\bullet} = h^{\bullet}$,[63, 64] with polaron hopping taking place on the B-O-B chains along corner-sharing-octahedra in the perovskite lattice.

In a Sr-doped lanthanum chromite $La_{1-x}Sr_xCrO_{3-\delta}$, the concentration in Cr^{4+} and thus hole concentration is governed by the concentration in Sr^{2+} at high pO_2.[65] G. J. Zhang et al. reported that on lanthanum chromites the Ni doping on the B-site has an enhancing effect on the conductivity by promoting Cr^{4+}. They demonstrated that the electric conductivity is directly proportional to the concentration of Cr^{4+}, which was enhanced for the doped-chromite $La_{0.9}Ca_{0.1}Cr_{0.5}Ni_{0.5}O_3$ in contrast to the $La_{0.9}Ca_{0.1}CrO_3$,[67] due to charge disproportionation of B-site cations according to:

$$Ni_{Cr}^{\times} + Cr_{Cr}^{\times} \rightarrow Ni_{Cr}' + Cr_{Cr}^{\bullet} \quad (6)$$

In L65SCN, following reactions may take place upon exposure to low pO_2:

$$2\ Cr_{Cr}^{\bullet} + O_O^{\times} \rightarrow 2Cr_{Cr}^{\times} + \frac{1}{2}O_2 + V_O^{\bullet\bullet} \quad (7)$$

$$2\ Ni_{Cr}^{\times} + O_O^{\times} \rightarrow 2Ni_{Cr}' + \frac{1}{2}O_2 + V_O^{\bullet\bullet} \quad (8)$$

Whereas the nickel cation undergoes reduction to its metallic state:[8]

$$Ni_{Cr}' + O_O^{\times} \rightarrow Ni^0 + \frac{1}{2}O_2 + V_{Cr}''' + V_O^{\bullet\bullet} \quad (9)$$

This phenomenon of Ni exsolution and thus Ni depletion of the perovskite lattice creates B-site vacancies that are not thermodynamically stable due to the nominally-A-Site deficient initial composition. Thereby, A- and B-site vacancies may recombine at the perovskite surface through the annihilation of ABO_3 unit cells, reducing the under stoichiometry on the A-site, such as:

$$V_{La}''' + V_{Cr}''' + 3V_O^{\bullet\bullet} \rightarrow nil \quad (10)$$

Considering the nominal A-site defficiency of the L65SCrN, the electroneutrality of the lattice is written as:

$$3\,[V_{La}'''] + [Sr_{La}'] + [Ni_{Cr}'] + 3[V_{Cr}'''] = [Cr_{Cr}^{\bullet}] + 2\,[V_O^{\bullet\bullet}] \quad (11)$$

$$[Cr_{Cr}^{\bullet}] = 3\,[V_{La}'''] + [Sr_{La}'] + [Ni_{Cr}'] + 3[V_{Cr}'''] - 2\,[V_O^{\bullet\bullet}] \quad (12)$$

Therefore, qualitatively, upon exsolution the decrement of Ni^{2+} (Ni_{Cr}') cations and A-site vacancies (V_{La}'''), will reduce concentration of $Cr_{Cr}^{\bullet}$, which may thus be detrimental for the conductivity. However, the detailed investigation of the point defect chemistry of the L65SCrN goes beyond the scope of this work.

About the role of the exsolved metallic nickel nanoparticles on the conductivity of L65SCrN, it is possible to assume that since they are isolated from each other, they cannot form a Ni-percolant network, leading to a marginal impact on the electronic conductivity. This may be explained by the discrete distributon of the Ni nanoparticles on the perovskite surface as shown in our previous work.[8] Therefore, it is likely that the exsolved Ni nanoparticles on the L65SCrN perovskite are not deciding for the conductivity, but rather that their role is mainly catalytical, by assiting the reaction kinectics with the hydrogen spillover process and H_2 desorption in SOE operation.

The extent of the conductivity change over time was evaluated by performing Van-der-Pauw measurements of the electronic in-plane conductivity of porous L65SCN films on insulating substrates in humid H_2 atmospheres for ~ 750 hours, as shown in Figure 7c. Once the temperature was stabilized at ~ 860°C and the pO_2 at ~ 10^{-16} bar, the initial conductivity was measured to be ca. 0.32 S•cm^{-1}, which served as the initial value for this durability test. During the first ~ 257 hours, the conductivity decreased to a value of ca. 0.24 S•cm^{-1}. Shortly after that, 10 redox cycles were performed (each lasting about one hour; see hour

~ 263-285 in Figure 7c) in order to evaluate if the conductivity recovered. Nevertheless, a slow conductivity degradation to a value of ~ 0.10 S•cm^{-1} for the total testing time of ~ 750 hours was observed, for which the redox cycles did not recover the initial conductivity.

Similar to the redox cycle performed on the 1000 hours-cell test, the conductivity of the L65SCrN did neither recover nor severely deteriorate after redox cycling. The overall rather slow trend towards lower effective conductivity and increased ohmic resistance indicates that the underlying reaction mechanism must involve a kinetically slow process, which includes cation diffusion. During an oxidation cycle, oxygen ions diffusion into the lattice is possible much faster. This was observed by Yasuda and Hishinuma, who reported the fractional conductivity change versus time by abruptly changing the pO_2 on $La_{0.65}Sr_{0.35}CrO_{3-\delta}$ samples at 1000 °C.[64] They modelled this behaviour as a non-steady state diffusion process, for which the driving force was considered as the oxygen exchange between the sample and the surrounding. After 2500 seconds, they observed that the conductivity stabilized at a constant value.[64] From their observations, it is possible to assume that for the L65SCrN perovskite, the duration of the redox cycles (each of 3600 seconds) were long enough for filling the oxygen vacancies, but very likely were not long enough for the Ni cations diffusion within the lattice, which would take possible longer times at higher temperatures.

Hence, we suspect that the degradation is likely to be influenced by the modification of the L65SCrN lattice chemistry, likely due to the exsolution of Ni, leading to changes of the charge carrier concentration. Taken together, these results suggest that the observed ohmic degradation at the cell level possibly originates from a degradation of the electronic conductivity of the L65SCrN. The various phenomena mentioned before are likely to act in synergy causing this long-term degradation.

However, we cannot unambiguously estimate in this work which one is indeed the most relevant effect. In general, we could assume that upon reduction of the L65SCrN, there is a trade-off between the amount of Ni on the B-site, that enhances the catalytic activity, and the deterioration of the bulk transport properties. The oxygen vacancy formation would promote Ni exsolution, but from a certain amount of exsolved Ni and therefore Ni depletion from the perovskite lattice, the electronic conductivity of the perovskite would be decreased. Therefore, in general for MIEC electrocatalysts with exsolution of metallic nanoparticles, it

is challenging to estimate to which extent the reduction of the B-site cations affects the long-term stability of the electronic conductivity, which may be unveiled by the ohmic degradation evolution over time. Notwithstanding, an additional contribution to the ohmic degradation observed in this study from the electrolyte and the barrier layers may not be excluded (Eq. 5).

3.5 Towards steam SOE operation without hydrogen on the feed gas. In this work, it was also investigated whether L65SCrN fuel electrodes are suitable for steam electrolysis without hydrogen sweep feed, not only at 860 °C but also at lower temperatures, i. e. 800 °C. Therefore, we performed tests on the same cell from the previous section at 860 °C and 800 °C with a fuel gas composition of 50% H_2O – 50% N_2 at -0.25 A•cm^{-2}. Polarization curves and 70 hours-durability tests are shown in Figure 8. Analogous to Figure 5, during the first 10 hours of operation an activation of the fuel electrode was observed, which was more pronounced at 860 °C. A voltage drift of 30 mV/1000 h was determined at 860 °C, while at 800 °C the drift was 15 mV/1000 h. In this case, it is reasonable to estimate a possible degradation in terms of an ohmic drift since the applied electrolysis current density was constant for both operating temperatures. With the observed voltage drift and the Ohm's law expressed as $\Delta U = J * \Delta ASR_{Total}$, the degradation could be calculated as:

$$\Delta ASR_{Total,860\,°C} = \frac{\Delta U_{860\,°C}}{J} = \frac{0.03\,V}{0.25\,A \cdot cm^{-2}} = 0.12\,\Omega \cdot cm^2 \qquad (13)$$

$$\Delta ASR_{Total,800\,°C} = \frac{\Delta U_{800\,°C}}{J} = \frac{0.015\,V}{0.25\,A \cdot cm^{-2}} = 0.06\,\Omega \cdot cm^2 \qquad (14)$$

What stands out from these results is the advantage of operating below 860 °C in terms of the ASR_{Total} degradation. Figure 8b reveals that there has been a slight increase in the measured voltage for the test at 800 °C in contrast to the drift observed at 860 °C, which is greater by a factor of 2. These results indicate that operation at lower temperatures would reduce the ASR_{Total} degradation and therefore would also reduce the drift in voltage on durability test in SOE operation. This is also consistent with a diffusion-limited degradation process.

As an opening to steam electrolysis without hydrogen on the feed gas, the L65SCrN perovskite could be considered a promising fuel electrode for the production of green hydrogen at ~ 800 °C. This operation mode would avoid the need of a reducing gas in the fuel feed in order to keep the electrode chemically reduced. Even so, further long-term investigations at different temperatures (lower than 860 °C) and also different electrolysis current densities would be required in order to better evaluate these perovskite fuel electrodes.

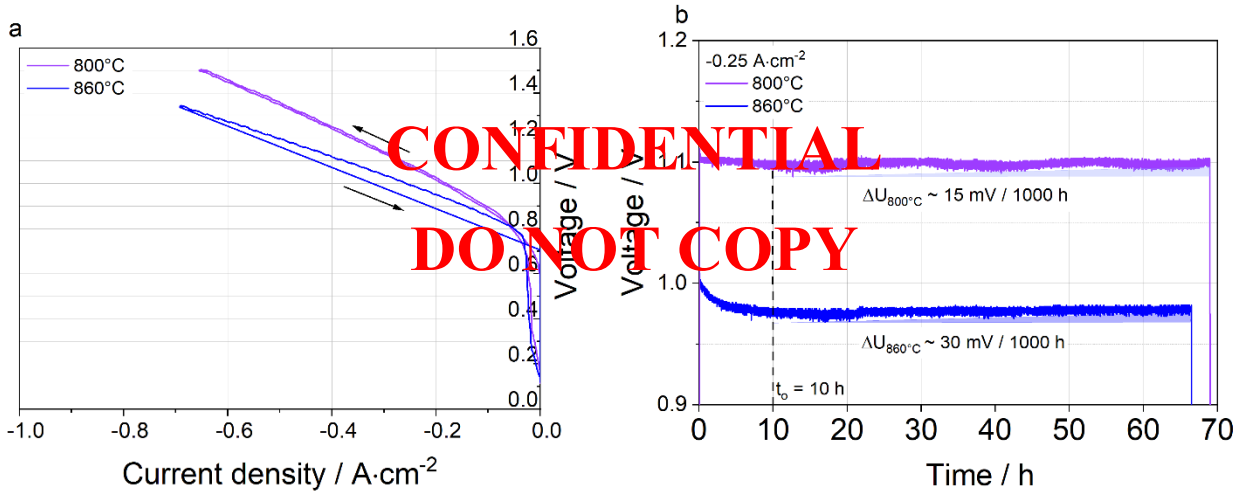

Figure 8. (a) Polarization curves at 860 °C and 800 °C in SOE of a full ESC with L65SCrN fuel electrode with fuel gas mixture of 50% H_2O - 50% N_2 (0.5 slpm of H_2O and 0.5 slpm of N_2). (b) Voltage vs. time during 70h-durability test in steam electrolysis with fuel gas mixture of 50% N_2 - 50% H_2O, with a fixed current density of -0.25 A·cm^{-2} at 860 °C (blue data) and 800 °C (purple data).

4. CONCLUSIONS

L65SCrN and Ni-CGO fuel electrodes were investigated for SOE operation at different temperatures in ESC architecture. Estimations of the specific energy consumption and the produced hydrogen rate normalized by the active area of the cells confirmed similar performance at 860 °C. However, L65SCrN-based cells showed a performance gain at lower temperatures. The temperature dependency of the ASR_{total} and the specific resistance of the perovskite fuel electrode surface process, in full and symmetrical cell configurations respectively, demonstrated lower apparent activation energy barrier values E_a in contrast to

the Ni-CGO cermets. This possibly finds its origin with a superior catalytic behavior of the L65SCrN over the Ni-CGO below 860 °C. With the proposed reaction model for water splitting and hydrogen formation, it was possible to assume that the role of the exsolved Ni nanoparticles is mainly catalytic. It is very likely that the metallic Ni assists the hydrogen spillover and H_2 desorption on the L65SCrN perovskite surface for the production of green hydrogen from water electrolysis at high temperatures.

During a 1000 hours-test at 860 °C in SOE operation, the L65SCrN-based cell showed a significant degradation of 48 mV /1000 h, for which an increment by 9.4 % of the ohmic resistance over time was identified. This degradation was possibly related to cation diffusion, which may affect the transport properties of the perovskite electrode. These outcomes may raise the question of how stable is this perovskite electrode in SOE operation and if other operation modes, such as co-electrolysis would be less detrimental for the transport properties. Also, lowering the operating temperature from 860 °C to 800 °C could be a suitable approach to mitigate degradation issues.

From an operational point of view, L65SCrN electrodes could also be operated in pure steam electrolysis, which can avoid the requirement of sweeping steam with hydrogen. This may facilitate system design and operation, as well as decreasing operational costs. The performance gain observed with temperature decrement for the perovskite electrode could be beneficial for the operation at larger scales. At the stack level, where temperature gradients are significant, the use of perovskite fuel electrodes may yield a more homogeneous performance between the different repeating units. This effect could be particularly favorable in cell architectures with lower ohmic contribution of the electrolyte. For instance, in CSC or metal supported cell architectures, being beneficial in terms of dynamic operation. Nevertheless, a key challenge remains to be the development and identification of MIEC materials that are more stable.

Beyond the specific case of this chromite, further experiments using other perovskite compositions that are more stable over time, as well as different cell architectures, could shed more light on the benefit of their implementation into cells and stacks for application in SOE systems.

Supporting Information. Additional SEM images of ceramic powders, Nyquist plots of full ESCs tested in SOE operation, equivalent circuit model (ECM) fittings, EDS analyses and XRD spectra are included in the supporting information (SI) file.

Corresponding Authors

* E-Mail: diana.amayaduenas@dlr.de ; remi.costa@dlr.de

Author Contributions

The manuscript was written through contributions of all authors. All authors have given approval to the final version of the manuscript.

Funding Sources

The German Academic Exchange Service (DAAD) is acknowledged for the Ph.D. scholarship of Ms. Diana-María Amaya-Dueñas with the award DLR/DAAD Research Fellowships – Doctoral Studies, 2017. Part of this work received funding from the German Federal Ministry of Education and Research (BMBF) within the Kopernikus Project P2X (Grant n03SFKE20).

Notes

The authors declare no competing financial interest.

ACKNOWLEDGMENTS

The German Academic Exchange Service (DAAD) is acknowledged for the Ph.D. scholarship of Ms. Diana-María Amaya-Dueñas with the award DLR/DAAD Research Fellowships – Doctoral Studies, 2017. Günter Roth and Dr. Robert Ruckdäschel are acknowledged for the SEM sample preparation and analyses, as well as Dr. Noriko Sata for the XRD measurements and Dr. Feng Han for his support on the sample cutting and preparation for the conductivity measurements. We are grateful to Prof. Dr. Jürgen Fleig from the Institute of Chemical Technologies and Analytics at TU Wien for the support with this collaboration. Part of this work received funding from the German Federal Ministry of Education and Research (BMBF) within the Kopernikus Project P2X (Grant n03SFKE20).

REFERENCES

1. *The National Hydrogen Strategy*; Federal Ministry for Economic Affairs and Energy Berlin, June 2020.
2. Hauch, A.; Kungas, R.; Blennow, P.; Hansen, A. B.; Hansen, J. B.; Mathiesen, B. V.; Mogensen, M. B., Recent advances in solid oxide cell technology for electrolysis. *Science* **2020,** *370* (6513).
3. Andreas Friedrich; Marcelo Carmo; Martin Müller; Tom Smolinka; André Weber; Falk Harnisch; Andreas Brinner; Marc Simon Löffler; Jörissen, L. In *Von der Elektrolyse zur Brenntoffzelle*, FVEE – Jahrestagung 2019: Energy Research for Future – Forschung für die Herausforderungen der Energiewende, 2019.
4. Mogensen, M. B.; Chen, M.; Frandsen, H. L.; Graves, C.; Hansen, J. B.; Hansen, K. V.; Hauch, A.; Jacobsen, T.; Jensen, S. H.; Skafte, T. L.; Sun, X., Reversible solid-oxide cells for clean and sustainable energy. *Clean Energy* **2019,** *3* (3), 175-201.
5. Qi, H.; Lee, Y.-L.; Yang, T.; Li, W.; Li, W.; Ma, L.; Hu, S.; Duan, Y.; Hackett, G. A.; Liu, X., Positive Effects of H2O on the Hydrogen Oxidation Reaction on Sr2Fe1.5Mo0.5O6−δ-Based Perovskite Anodes for Solid Oxide Fuel Cells. *ACS Catalysis* **2020,** *10* (10), 5567-5578.
6. Ebbesen, S. D.; Mogensen, M., Electrolysis of carbon dioxide in Solid Oxide Electrolysis Cells. *Journal of Power Sources* **2009,** *193* (1), 349-358.
7. Peters, R.; Deja, R.; Blum, L.; Nguyen, V. N.; Fang, Q.; Stolten, D., Influence of operating parameters on overall system efficiencies using solid oxide electrolysis technology. *International Journal of Hydrogen Energy* **2015,** *40* (22), 7103-7113.
8. Amaya-Dueñas, D.-M.; Chen, G.; Weidenkaff, A.; Sata, N.; Han, F.; Biswas, I.; Costa, R.; Friedrich, K. A., A–site Deficient Chromite with In Situ Ni Exsolution as Fuel Electrode for Solid Oxide Cells (SOC). *Journal of Materials Chemistry A* **2021,** *9*, 5685-5701.
9. Riegraf, M.; Zekri, A.; Knipper, M.; Costa, R.; Schiller, G.; Friedrich, K. A., Sulfur poisoning of Ni/Gadolinium-doped ceria anodes: A long-term study outlining stable solid oxide fuel cell operation. *Journal of Power Sources* **2018,** *380*, 26-36.
10. Knibbe, R.; Wang, J.-J.; Blennow, P.; Thydén, K.; Persson, Å. H.; Mikkelsen, L.; Klemensø, T., Oxidation in ceria infiltrated metal supported SOFCs – A TEM investigation. *Journal of Power Sources* **2013,** *228*, 75-82.
11. Hoerlein, M. P.; Riegraf, M.; Costa, R.; Schiller, G.; Friedrich, K. A., A parameter study of solid oxide electrolysis cell degradation: Microstructural changes of the fuel electrode. *Electrochimica Acta* **2018,** *276*, 162-175.
12. Tietz, F.; Sebold, D.; Brisse, A.; Schefold, J., Degradation phenomena in a solid oxide electrolysis cell after 9000 h of operation. *Journal of Power Sources* **2013,** *223*, 129-135.
13. Chen, J.; Ouyang, M.; Boldrin, P.; Atkinson, A.; Brandon, N. P., Understanding the Coarsening and Degradation in a Nanoscale Nickel Gadolinia-Doped-Ceria Electrode for High-Temperature Applications. *ACS Applied Materials & Interfaces* **2020,** *12* (42), 47564-47573.
14. Holzer, L.; Iwanschitz, B.; Hocker, T.; Münch, B.; Prestat, M.; Wiedenmann, D.; Vogt, U.; Holtappels, P.; Sfeir, J.; Mai, A.; Graule, T., Microstructure degradation of cermet anodes for solid oxide fuel cells: Quantification of nickel grain growth in dry and in humid atmospheres. *Journal of Power Sources* **2011,** *196* (3), 1279-1294.
15. Chen, G.; Guan, G.; Kasai, Y.; Abudula, A., Nickel volatilization phenomenon on the Ni-CGO anode in a cathode-supported SOFC operated at low concentrations of H2. *International Journal of Hydrogen Energy* **2012,** *37* (1), 477-483.

16. Mogensen, M. B.; Hauch, A.; Sun, X.; Chen, M.; Tao, Y.; Ebbesen, S. D.; Hansen, K. V.; Hendriksen, P. V., Relation Between Ni Particle Shape Change and Ni Migration in Ni–YSZ Electrodes – a Hypothesis. **2017,** *17* (4), 434-441.
17. Jiao, Z.; Busso, E. P.; Shikazono, N., Influence of Polarization on the Morphological Changes of Nickel in Fuel Electrodes of Solid Oxide Cells. *Journal of The Electrochemical Society* **2020,** *167* (2), 024516.
18. Nakajo, A.; Rinaldi, G.; Caliandro, P.; Jeanmonod, G.; Navratilova, L.; Cantoni, M.; Van herle, J., Evolution of the Morphology Near Triple-Phase Boundaries in Ni–Yttria Stabilized Zirconia Electrodes Upon Cathodic Polarization. *Journal of Electrochemical Energy Conversion and Storage* **2020,** *17* (4).
19. Song, B.; Bertei, A.; Wang, X.; Cooper, S. J.; Ruiz-Trejo, E.; Chowdhury, R.; Podor, R.; Brandon, N. P., Unveiling the mechanisms of solid-state dewetting in Solid Oxide Cells with novel 2D electrodes. *Journal of Power Sources* **2019,** *420*, 124-133.
20. Faes, A.; Hessler-Wyser, A.; Zryd, A.; Van Herle, J., A Review of RedOx Cycling of Solid Oxide Fuel Cells Anode. *Membranes (Basel)* **2012,** *2* (3), 585-664.
21. Duboviks, V.; Maher, R. C.; Kishimoto, M.; Cohen, L. F.; Brandon, N. P.; Offer, G. J., A Raman spectroscopic study of the carbon deposition mechanism on Ni/CGO electrodes during CO/CO2 electrolysis. *Phys. Chem. Chem. Phys.* **2014,** *16* (26), 13063-13068.
22. Agency, I. E. *The Role of Critical World Energy Outlook Special Report Minerals in Clean Energy Transitions*; International Energy Agency: 2021.
23. Holtappels, P.; Ramos, T.; Tietz, F.; Malzbender, J.; Mai, A.; Hansen, J. R.-.; Irvine, J. T. S. *Sulphur, Carbon, and re-Oxidation Tolerant Anodes and Anode Supports for Solid Oxide Fuel Cells*; European Commision 2015.
24. Zhu, H.; Zhang, P.; Dai, S., Recent Advances of Lanthanum-Based Perovskite Oxides for Catalysis. *ACS Catalysis* **2015,** *5* (11), 6370-6385.
25. Myung, J.-h.; Neagu, D.; Miller, D. N.; Irvine, J. T. S., Switching on electrocatalytic activity in solid oxide cells. *Nature* **2016,** *537* (7621), 528-531.
26. Tsekouras, G.; Neagu, D.; Irvine, J. T. S., Step-change in high temperature steam electrolysis performance of perovskite oxide cathodes with exsolution of B-site dopants. *Energy Environ. Sci.* **2013,** *6* (1), 256-266.
27. Kyriakou, V.; Neagu, D.; Papaioannou, E. I.; Metcalfe, I. S.; van de Sanden, M. C. M.; Tsampas, M. N., Co-electrolysis of H2O and CO2 on exsolved Ni nanoparticles for efficient syngas generation at controllable H2/CO ratios. *Applied Catalysis B: Environmental* **2019,** *258*, 117950.
28. Opitz, A. K.; Nenning, A.; Rameshan, C.; Kubicek, M.; Gotsch, T.; Blume, R.; Havecker, M.; Knop-Gericke, A.; Rupprechter, G.; Klotzer, B.; Fleig, J., Surface Chemistry of Perovskite-Type Electrodes During High Temperature CO2 Electrolysis Investigated by Operando Photoelectron Spectroscopy. *ACS Appl Mater Interfaces* **2017,** *9* (41), 35847-35860.
29. Sapountzi, F. M.; Brosda, S.; Papazisi, K. M.; Balomenou, S. P.; Tsiplakides, D., Electrochemical performance of La0.75Sr0.25Cr0.9M0.1O3 perovskites as SOFC anodes in CO/CO2 mixtures. *Journal of Applied Electrochemistry* **2012,** *42* (9), 727-735.
30. Neagu, D.; Kyriakou, V.; Roiban, I.-L.; Aouine, M.; Tang, C.; Caravaca, A.; Kousi, K.; Schreur-Piet, I.; Metcalfe, I. S.; Vernoux, P.; van de Sanden, M. C. M.; Tsampas, M. N., In Situ Observation of Nanoparticle Exsolution from Perovskite Oxides: From Atomic Scale Mechanistic Insight to Nanostructure Tailoring. *ACS Nano* **2019,** *13* (11), 12996-13005.

31. Matthias Riegraf; Diana M. Amaya-Dueñas; Noriko Sata; K. Andreas Friedrich; Costa, R., Performance and Limitations of Nickel-Doped Chromite Anodes in Electrolyte-Supported Solid Oxide Fuel Cells. *ChemSusChem* **2021,** *14*, 2401-2413.
32. Nenning, A.; Bischof, C.; Fleig, J.; Bram, M.; Opitz, A. K., The Relation of Microstructure, Materials Properties and Impedance of SOFC Electrodes: A Case Study of Ni/GDC Anodes. *Energies* **2020,** *13* (4).
33. Nenning, A.; Holzmann, M.; Fleig, J.; Opitz, A. K., Excellent kinetics of single-phase Gd-doped ceria fuel electrodes in solid oxide cells. *Materials Advances* **2021,** *2* (16), 5422-5431.
34. Johnson, D. *ZView Electrochemical Impedance Software*, 2.3b; Scribner Associates, Inc.: 2000.
35. Van Der Pauw, L. J., A Method of Measuring the Resistivity and Hall Coefficient on Lamellae of Arbitrary Shape. *Philips Technical Review* **1958,** *20*, 220-224.
36. Perry, S. C.; Ponce de León, C.; Walsh, F. C., Review—The Design, Performance and Continuing Development of Electrochemical Reactors for Clean Electrosynthesis. *Journal of The Electrochemical Society* **2020,** *167* (15).
37. Sunfire, Sunfire HyLink. In *SUNFIRE-HYLINK HL40*, GmbH, S., Ed.
38. Amaya-Dueñas, D.-M.; Riedel, M.; Riegraf, M.; Costa, R.; Friedrich, K. A., High Temperature Co-electrolysis for Power-to-X. *Chemie Ingenieur Technik* **2020,** *92* (1-2), 45-52.
39. Klotz, D. Characterization and Modeling of Electrochemical Energy Conversion Systems by Impedance Techniques. Karlsruher Instituts für Technologie (KIT), Karlsruhe, 2012.
40. Schefold, J.; Brisse, A.; Surrey, A.; Walter, C., 80,000 current on/off cycles in a one year long steam electrolysis test with a solid oxide cell. *International Journal of Hydrogen Energy* **2020,** *45* (8), 5143-5154.
41. Opitz, A. K.; Gerstl, M.; Bram, M., Model System Supported Impedance Simulation of Composite Electrodes. *Fuel Cells* **2014,** *14* (4), 417-428.
42. Adler, S. B. L., J.A.; Steele, B.C.H, Electrode Kinetics of Porous Mixed-Conducting Oxygen Electrodes. *J. Electrochem. Soc* **1996,** *143*, 3554–3564.
43. Yurkiv, V.; Costa, R.; Ivan, Z.; Ansar, A.; Bessler, W. G., Impedance of the Surface Double Layer of LSCF/CGO Composite Cathodes: An Elementary Kinetic Model. *Journal of The Electrochemical Society* **2014,** *161* (4), F480-F492.
44. Njodzefon, J.-C.; Graves, C. R.; Mogensen, M. B.; Weber, A.; Hjelm, J., Kinetic Studies on State of the Art Solid Oxide Cells: A Comparison between Hydrogen/Steam and Reformate Fuels. *Journal of The Electrochemical Society* **2016,** *163* (13), F1451-F1462.
45. Bessler, W. G. G., Stefan Gas Concentration Impedance of Solid Oxide Fuel Cell Anodes II. Channel Geometry. *J. Electrochem. Soc* **2007,** *154*, B548-B559.
46. Schefold, J.; Brisse, A.; Poepke, H., Long-term Steam Electrolysis with Electrolyte-Supported Solid Oxide Cells. *Electrochimica Acta* **2015,** *179*, 161-168.
47. Riegraf, M.; Yurkiv, V.; Costa, R.; Schiller, G.; Friedrich, K. A., Evaluation of the Effect of Sulfur on the Performance of Nickel/Gadolinium-Doped Ceria Based Solid Oxide Fuel Cell Anodes. **2017,** *10* (3), 587-599.
48. Nielsen, J.; Klemensø, T.; Blennow, P., Detailed impedance characterization of a well performing and durable Ni:CGO infiltrated cermet anode for metal-supported solid oxide fuel cells. *Journal of Power Sources* **2012,** *219*, 305-316.
49. Riegraf, M.; Costa, R.; Schiller, G.; Friedrich, K. A.; Dierickx, S.; Weber, A., Electrochemical Impedance Analysis of Symmetrical Ni/Gadolinium-Doped Ceria (CGO10)

Electrodes in Electrolyte-Supported Solid Oxide Cells. *Journal of The Electrochemical Society* **2019,** *166* (13), F865-F872.
50. Nenning, A.; Volgger, L.; Miller, E.; Mogni, L. V.; Barnett, S.; Fleig, J., The Electrochemical Properties of Sr(Ti,Fe)O3-δfor Anodes in Solid Oxide Fuel Cells. *Journal of The Electrochemical Society* **2017,** *164* (4), F364-F371.
51. Velicsanyi, P.; Gerstl, M.; Nenning, A.; Hutter, H.; Fleig, J.; Opitz, A. K., The Effect of Mn Co-doping on the Electrochemical Properties of $Gd_{0.2}Ce_{0.8}O_{1.9-\delta}$/Pt Model-composite Electrodes. *ECS Transactions* **2015,** *68*, 1509-1516.
52. Jung, W.; Dereux, J. O.; Chueh, W. C.; Hao, Y.; Haile, S. M., High electrode activity of nanostructured, columnar ceria films for solid oxide fuel cells. *Energy & Environmental Science* **2012,** *5* (9).
53. Liu, L.; Kim, G.-Y.; Chandra, A., Modeling of Ni–CGO anode in a solid oxide fuel cell deposited by spray pyrolysis. *Journal of Power Sources* **2012,** *210*, 129-137.
54. Opitz, A. K.; Nenning, A.; Vonk, V.; Volkov, S.; Bertram, F.; Summerer, H.; Schwarz, S.; Steiger-Thirsfeld, A.; Bernardi, J.; Stierle, A.; Fleig, J., Understanding electrochemical switchability of perovskite-type exsolution catalysts. *Nat Commun* **2020,** *11* (1), 4801.
55. Opitz, A. K.; Nenning, A.; Rameshan, C.; Rameshan, R.; Blume, R.; Havecker, M.; Knop-Gericke, A.; Rupprechter, G.; Fleig, J.; Klotzer, B., Enhancing electrochemical water-splitting kinetics by polarization-driven formation of near-surface iron(0): an in situ XPS study on perovskite-type electrodes. *Angew Chem Int Ed Engl* **2015,** *54* (9), 2628-32.
56. Zhu, T.; Troiani, H. E.; Mogni, L. V.; Han, M.; Barnett, S. A., Ni-Substituted Sr(Ti,Fe)O3 SOFC Anodes: Achieving High Performance via Metal Alloy Nanoparticle Exsolution. *Joule* **2018,** *2* (3), 478-496.
57. Feng, Z. A.; El Gabaly, F.; Ye, X.; Shen, Z. X.; Chueh, W. C., Fast vacancy-mediated oxygen ion incorporation across the solid–gas electrochemical interface. *Nat Commun* **2014,** *5*, 4374.
58. Nenning, A.; Navickas, E.; Hutter, H.; Fleig, J., Water-Induced Decoupling of Tracer and Electrochemical Oxygen Exchange Kinetics on Mixed Conducting Electrodes. *J Phys Chem Lett* **2016,** *7* (14), 2826-31.
59. Hansen, H. A.; Wolverton, C., Kinetics and Thermodynamics of H2O Dissociation on Reduced CeO2(111). *The Journal of Physical Chemistry C* **2014,** *118* (47), 27402-27414.
60. Gu, X.-K.; Nikolla, E., Fundamental Insights into High-Temperature Water Electrolysis Using Ni-Based Electrocatalysts. *The Journal of Physical Chemistry C* **2015,** *119* (48), 26980-26988.
61. Mizusaki, J.; Yonemura, Y.; Kamata, H.; Ohyama, K.; Mori, N.; Takai, H.; Tagawa, H.; Dokiya, M.; Naraya, K.; Sasamoto, T.; Inaba, H.; Hashimoto, T., Electronic conductivity, Seebeck coefficient, defect and electronic structure of nonstoichiometric La1−xSrxMnO3. *Solid State Ionics* **2000,** *132* (3), 167-180.
62. Jiang, S. P.; Liu, L.; Ong, K. P.; Wu, P.; Li, J.; Pu, J., Electrical conductivity and performance of doped LaCrO3 perovskite oxides for solid oxide fuel cells. *Journal of Power Sources* **2008,** *176* (1), 82-89.
63. Sauvet, A. L.; Irvine, J. T. S., Catalytic activity for steam methane reforming and physical characterisation of La1−xSrxCr1−yNiyO3−δ. *Solid State Ionics* **2004,** *167* (1), 1-8.
64. Yasuda, I.; Hishinuma, M., Electrical conductivity and chemical diffusion coefficient of Sr-doped lanthanum chromites. *Solid State Ionics* **1995,** *80* (1), 141-150.

65. Meadowcroft, D. B., Some properties of strontium-doped lanthanum chromite. *Journal of Physics D: Applied Physics* **1969,** *2* (9), 1225-1233.
66. Tjaden, B.; Brett, D. J. L.; Shearing, P. R., Tortuosity in electrochemical devices: a review of calculation approaches. *International Materials Reviews* **2018,** *63* (2), 47-67.
67. Zhang, G. J.; Song, Y. W.; Xiong, H.; Zheng, J. Y.; Jia, Y. Q., Synthesis and crystal structure of La0.9Ca0.1Cr1−xNixO3 (x = 0.0–1.0) and electric conductivity of La0.9Ca0.1Cr0.5Ni0.5O3. *Materials Chemistry and Physics* **2002,** *73* (1), 101-105.